Atmos. Chem. Phys., 12, 653–667, 2012
www.atmos-chem-phys.net/12/653/2012/
doi:10.5194/acp-12-653-2012

Atmospheric Chemistry and Physics

Combining Bayesian methods and aircraft observations to constrain the $HO^{\cdot}$ + NO_2 reaction rate

B. H. Henderson[1,2], R. W. Pinder[2], J. Crooks[3], R. C. Cohen[4], A. G. Carlton[5], H. O. T. Pye[2], and W. Vizuete[1]

[1]Department of Environmental Science and Engineering, University of North Carolina, Chapel Hill, NC, USA
[2]National Exposure Research Laboratory, US Environmental Protection Agency (USEPA), RTP, NC, USA
[3]National Health and Environmental Effects Research Laboratory, US Environmental Protection Agency (USEPA), RTP, NC, USA
[4]Departments of Chemistry and Earth and Planetary Sciences, University of California, Berkeley, CA, USA
[5]Department of Environmental Sciences, Rutgers, New Brunswick, NJ, USA

Correspondence to: B. H. Henderson (barronh@gmail.com)

Received: 18 July 2011 – Published in Atmos. Chem. Phys. Discuss.: 29 August 2011
Revised: 6 December 2011 – Accepted: 5 January 2012 – Published: 16 January 2012

Abstract. Tropospheric ozone is the third strongest greenhouse gas, and has the highest uncertainty in radiative forcing of the top five greenhouse gases. Throughout the troposphere, ozone is produced by radical oxidation of nitrogen oxides ($NO_x = NO + NO_2$). In the upper troposphere (8–10 km), current chemical transport models under-estimate nitrogen dioxide (NO_2) observations. Improvements to simulated NO_x production from lightning have increased NO_2 predictions, but the predictions in the upper troposphere remain biased low. The upper troposphere has low temperatures ($T < 250$ K) that increase the uncertainty of many important chemical reaction rates. This study constrains uncertain reaction rates by combining model predictions with measurements from the Intercontinental Chemical Transport Experiment-North America observational campaign. The results show that the nitric acid formation rate, which is the dominant sink of NO_2 and radicals, is currently over-estimated by 22 % in the upper troposphere. The results from this study suggest that the temperature sensitivity of nitric acid formation is lower than currently recommended. Since the formation of nitric acid removes nitrogen dioxide and radicals that drive the production of ozone, the revised reaction rate will affect ozone concentrations in upper troposphere impacting climate and air quality in the lower troposphere.

1 Introduction

Ozone in the upper troposphere is an efficient greenhouse gas (0.25–0.65 Wm^{-2}; Solomon et al., 2007) with a long chemical lifetime (100–365 days; Kley, 1997; Wang et al., 1998). In the troposphere, ozone (O_3) is produced by net photolysis of nitrogen dioxide (NO_2) shown in Reactions (R1–R3). NO_2 is produced by net oxidation of nitric oxide (NO) by peroxy radicals (e.g., R4 and R5). The peroxy radicals that drive oxidation are produced by photolysis (e.g., R6) or by oxidation of organics (e.g., R7 and R8). Radicals and nitrogen oxides ($NO_x = NO + NO_2$) can be temporarily removed from the cycling by production of reservoir species (e.g., peroxy nitrates) via thermally equilibrated Reactions (R9–R11). Radicals and NO_x are removed from the cycle primarily by hydroxyl radical ($HO^{\bullet}$) combination with NO_2 to produce nitric acid (R12). In the upper troposphere, hydrogen radicals ($HO_x = HO_2^{\bullet} + HO^{\bullet}$) are terminated primarily by nitric acid formation, net pernitric acid reactions (R11, R13), and by radical-radical reactions (e.g., R14).

$$NO_2 + h\nu \rightarrow NO + O^3P \quad \text{(R1)}$$

$$O^3P + O_2 \rightarrow O_3 \quad \text{(R2)}$$

$$NO + O_3 \rightarrow NO_2 + O_2 \quad \text{(R3)}$$

$$HO_2^{\bullet} + NO \rightarrow NO_2 + HO^{\bullet} \quad \text{(R4)}$$

$$CH_3O_2^{\bullet} + NO \rightarrow NO_2 + CH_3O^{\bullet} \quad \text{(R5)}$$

$$CH_2O + h\nu \rightarrow 2HO_2^{\bullet} + CO \quad \text{(R6)}$$

$$CH_4 + HO^{\bullet} \rightarrow CH_3O_2^{\bullet} + H_2O \quad \text{(R7)}$$

$$CH_3OOH + HO^{\bullet} \rightarrow 30\,\%\,(CH_2O + HO^{\bullet}) + 70\,\%\,CH_3O_2^{\bullet} \quad \text{(R8)}$$

$$CH_3C(O)O_2^{\bullet} + NO_2 \underset{k_e}{\overset{k_f}{\rightleftharpoons}} CH_3C(O)O_2NO_2 \quad \text{(R9)}$$

$$CH_3O_2^{\bullet} + NO_2 \underset{k_e}{\overset{k_f}{\rightleftharpoons}} CH_3O_2NO_2 \quad \text{(R10)}$$

$$HO_2^{\bullet} + NO_2 \underset{k_e}{\overset{k_f}{\rightleftharpoons}} HNO_4 \quad \text{(R11)}$$

$$NO_2 + HO^{\bullet} \rightarrow HNO_3 \quad \text{(R12)}$$

$$HNO_4 + HO^{\bullet} \rightarrow NO_2 + O_2 + H_2O \quad \text{(R13)}$$

$$HO_2^{\bullet} + HO^{\bullet} \rightarrow H_2O + O_2 \quad \text{(R14)}$$

The reactions that cycle NO_x and produce ozone each have uncertainty as reported in the literature. Each paper in the literature estimates a rate from observations of reactants or products in an experimental system. The authors repeat their experiments (potentially for multiple environmental conditions) to yield observations within a precision range specific to the experimental design. If multiple studies are available in the literature, the observations from each can be pooled to estimate the quantitative uncertainty. Often the uncertainty cannot be fully characterized by quantitative uncertainty, so panels of experts add their best estimates of the systematic uncertainty. The uncertainty of many reaction rates is summarized by Atkinson et al. (2004, hereafter IUPAC04), Atkinson et al. (2006, hereafter IUPAC06) and Sander et al. (2011, hereafter JPL11). The uncertainty of each reaction rate has a non-linear impact on model estimates of NO_x and ozone.

Models that predict NO_x and ozone use uncertain emissions, transport, and chemical reactions. For a model to accurately predict NO_x or ozone, the reactive cycling of NO_x must be in balance with the physical transport and emissions of radical precursors and NO_x. Model evaluations of NO_x, using data from the Intercontinental Chemical Transport Experiment-North America (INTEX-A) campaign, have shown a low-bias for simulated NO_2 using GEOS-Chem (Hudman et al., 2007). The NO_2 low-bias is consistent with other studies that found bias in the upper troposphere in the Community Multiscale Air Quality (Napelenok et al., 2008) or that box model biases required constraining radicals (Bertram et al., 2007).

The low-bias in simulated NO_2 has led to many studies addressing the uncertainty in the sources and sinks of NO_x. Hudman et al. (2007) showed that increasing NO_x production from lightning helped improve model performance for the INTEX-A period, but the simulated mean concentration ($\approx$300 ppt) was still about half of the observed mean ($\approx$600 ppt). Browne et al. (2011) found that the observations are overestimated in the upper troposphere due to an interference in the TD-LIF instrument from methyl peroxy nitrate ($CH_3O_2NO_2$). Allen et al. (2011) incorporated interference estimates and lightning NO_x production, but still found under-estimations of modeled NO_2 in the upper troposphere. Olson et al. (2006) and Ren et al. (2008) both identify chemical reactions as a potential source of uncertainty. Henderson et al. (2011) found that the chemistry representation of the global and regional models may cause a 30 % low-bias.

In this paper, we constrain uncertain reaction rates to improve the chemical mechanisms used in 3-dimensional models. To constrain reactions, we use Bayesian inference techniques that combine model predictions and observations to constrain reaction coefficients. We find evidence that the reaction coefficient for $NO_2 + HO^{\bullet}$ (R12) should be revised from the current literature values (IUPAC06; JPL11). The reaction rate for Reaction (R12) has recently been revised based on the work of Mollner et al. (2010), but that study was at a fixed temperature that cannot test the temperature sensitivity (i.e., $(T/300)^{-n}$ where literature values for n range from 2.67 to 2.97). This work identifies a temperature dependency that reduces the rate of R12 by 22 % at 241 K from current recommendations (an additional 12 % lower than Mollner et al., 2010). This temperature sensitivity needs to be confirmed in laboratory experiments.

2 Model framework

In this study, a combination of stochastic and deterministic modeling is used as the framework to constrain reaction rates. The model framework used here was originally developed by Henderson et al. (2011); the core framework and additions for this work are described below. The model framework relies on the convective turnover of the upper troposphere, or deep convection, that maintains a "persistent imbalance" (Prather and Jacob, 1997). Deep convection is associated with precipitation that removes water soluble HNO_3, but does not remove less soluble compounds including NO_x. These deep convection events may also be associated with lightning that produces NO_x (Jaeglé et al., 1998). The ratio of NO_x to HNO_3, therefore, can be used as a chemical indicator of recent convection (Bertram et al., 2007). This indicator is used to identify air parcels immediately following convection. Next, the model framework photochemically ages those parcels and stochastic transport algorithms simulate the removal of air parcels from the upper troposphere. Finally, the distribution of simulated air parcels can be compared to the distribution of observed air parcels.

Figure 1 shows that, following convection, air parcels chemically convert NO_x to HNO_3 while simultaneously being transported out of the upper troposphere (defined here as between 8 and 10 km). Each line in Fig. 1a represents the vertical motion of an air parcel immediately following

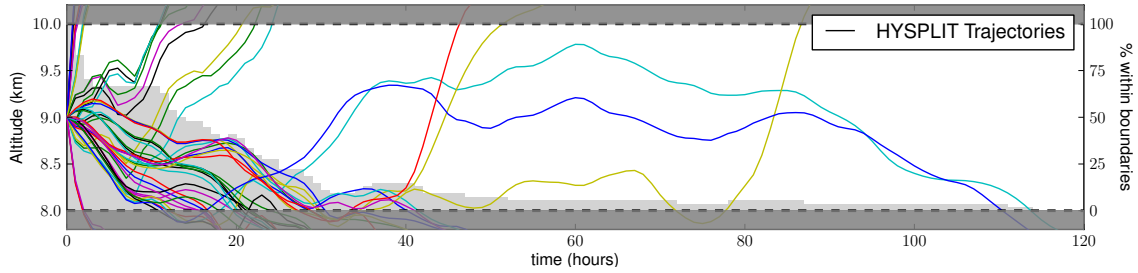

(a) Vertical Transport

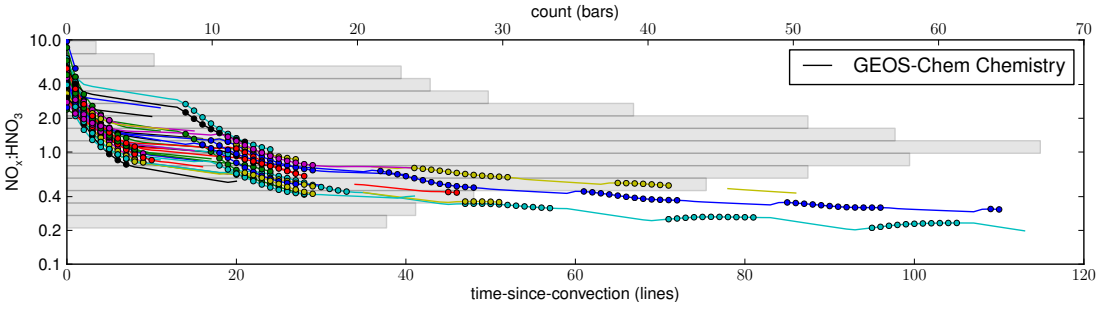

(b) Chemistry

Fig. 1. Conceptual model of vertical transport **(a)** and chemistry **(b)** of hypothetical air parcels following convection. Vertical transport following convection is characterized in **(a)** by 54 lines from HYSPLIT trajectories that include convective motion and isentropic subsidence. During transport, NO_x (and NO_2) is converted to HNO_3 by chemistry that is characterized by lines in **(b)** from GEOS-Chem simulations with night-time values in gray. Chemistry line segments are randomly paired with trajectories (by color) and hourly samples are included in the ensemble (represented by dots in **b**). Ensemble members can only be selected during the day when observations were taken, and while within the 8 to 10 km study boundaries. The ensemble has a distribution of NO_2:HNO_3 (bars in **b**) that is approximately log-normal.

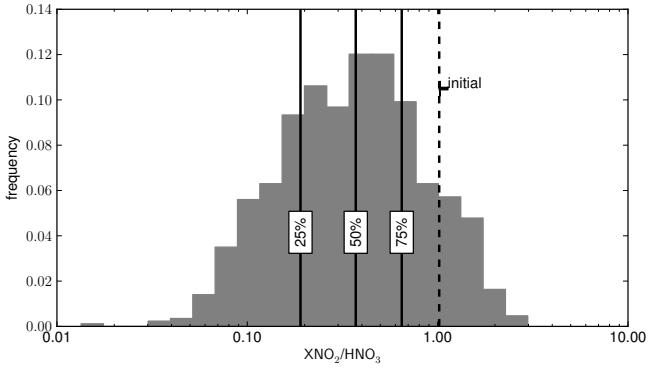

Fig. 2. Observed XNO_2 to HNO_3 ratio, from 8 to 10 km, with percentile markers (solid lines) and initial conditions threshold (dashed lines).

convection. During vertical motion, Fig. 1b shows that the air parcels convert NO_x to HNO_3. The air parcels in Fig. 1b are removed when the air parcel leaves the 8 to 10 km study area. While the air parcels are in the study area, they are available for sampling shown by dots.

2.1 Observations and initial conditions

The modeling framework starts with an observation-based initial condition. The observations used here are from the Intercontinental Chemical Transport Experiment-North America (INTEX-A) campaign. During INTEX-A the National Aeronautics and Space Administration (NASA) aircraft (DC-8) performed a suite of measurements that have been combined into a 10-s merged dataset. The air parcels to initialize the model can be identified by the ratio of highly soluble HNO_3 to NO_x. In this study, we use NO_2 instead of NO_x because the NO observation is less frequent. The NO_2 observation has been shown to have interferences from HNO_4 and methyl peroxy nitrate ($CH_3O_2NO_2$) (Browne et al., 2011). Due to these interferences, we refer to the NO_2 observation as XNO_2, and the model results incorporate the interference as described in the Appendix. The relative rates of physical removal and XNO_2 to HNO_3 conversion create a distribution of photochemically aged air parcels. During INTEX-A, the observed XNO_2 to HNO_3 ratio is log-normally distributed as shown in Fig. 2. The samples with the highest 12.5 % ($n = 65$) of XNO_2 to HNO_3 ratios are those parcels that most immediately follow convection and are selected to initialize simulated air parcels. Simulations are initialized with measurements of environmental conditions as well as inorganic,

organic, and particle composition. For each measurement used, descriptive statistics (median, mean, and standard deviation) are shown in Appendix A1, both for the whole dataset and for the initial conditions.

2.2 Photochemical processing

Each initial air parcel is the starting point for a deterministic photochemical model processed for 10 days. Photochemical processing includes gas-phase chemistry, partitioning to aerosols, and heterogeneous reactions. The gas-phase chemistry is simulated using the deterministic model used by GEOS-Chem "full" NO_x-hydrocarbon simulations (Mao et al., 2009) with the improvements suggested by Henderson et al. (2011). Additional reactions for $CH_3O_2NO_2$ have been added based on JPL11 with photolysis estimated using HNO_4 as a proxy (following Browne et al., 2011). To calculate photolysis rates, we use the Tropospheric Ultraviolet (TUV) version 4.6 (Madronich, 2002) to integrate actinic flux, cross sections and quantum yields. The TUV model (version 4.6) has been updated to include temperature-dependent cross sections and quantum yields for NO_2 and CH_2O recommended by IUPAC04 and IUPAC06. The partitioning of gas-phase species to aerosols is performed using the ISORROPIA II model (Fountoukis and Nenes, 2007). The heterogeneous reactions recommended in Jacob (2000) were also added to the framework. This includes heterogeneous formation of HNO_3 from N_2O_5 following Evans and Jacob (2005) (with sign correction detailed in Davis et al., 2008). The heterogeneous reactions were added to this modeling framework following the implementation in GEOS-Chem model version 9-01-01 (similar to the model used by Hudman et al., 2007).

The photochemical processing in this model is influenced by the environmental conditions: temperature, pressure, and relative humidity. The environmental conditions may rapidly change following deep convection due to convective scale subsidence and adiabatic warming. The initial conditions have lower pressure (6 %) and lower temperature (5 %) compared to the air parcels with NO_2:HNO_3 in the second quartile. In this study, pressure and temperature have been parameterized to adjust as they chemically age (see Appendix for details).

2.3 Physical removal

The chemical predictions are then stochastically post-processed to simulate transport. In the real world, air parcels are transported out of the upper troposphere (defined here as 8–10 km) by adiabatic motion, convective subsidence, and synoptic scale subsidence (as seen in Fig. 1a). We assume that the probability of being transported out of the upper troposphere (either above 10 or below 8 km) is a time independent process, and as such can be simulated by an exponential distribution (Gallager, 1996). To account for transport, a stochastic removal process probabilistically selects a decreasing number of air parcels to represent each output time-since-convection (hourly sampled). The exponential distribution is corrected (Henderson et al., 2011) to account for preferential sampling performed during the sampling campaign (Bertram et al., 2007; Fuelberg et al., 2007). The number of samples selected at any time can be calculated following Henderson et al. (2011, p. 280, Eq. 2). After stochastically selecting simulated air parcels, the remaining air parcels are an ensemble of that is representative of the upper troposphere. The air parcels included in this ensemble have varying initial conditions and time-since-convection. The only independent variable necessary to select air parcels is the average time-since-convection (τ).

The average time-since-convection (τ) is unknown, but is necessary to create an accurate representation of the upper troposphere. Increasing τ increases the relative probability of sampling older air parcels that have lower XNO_2 and higher HNO_3. So increasing (decreasing) τ, increases (decreases) the oxidation state of the prediction ensemble. Although the exact value of τ is unknown, the range can be constrained by evaluation of chemical simulations and meteorological back trajectories. By evaluating the back trajectories from Fuelberg et al. (2007), Henderson et al. (2011) estimated a τ range from 40 to 58 h. By evaluating the chemical simulations, Henderson et al. (2011) estimated a τ value for GEOS-Chem of 36 h. Because of the uncertainty in the τ value, the modeling framework will be evaluated at each average time-since-convection from 36 to 58 by one-hour intervals.

3 Uncertainty analysis

The model framework includes 296 reactions, each with continuous uncertainty, that each influences the model predictions. To reduce the number of reactions, reaction rates are pre-screened as described in Selecting Influential Variables below. For only the pre-screened variables, the uncertainty is constrained using Bayesian inference as described in Bayesian Updating below. These two steps will identify reaction rates whose uncertainty is key to understanding ozone precursors in the upper troposphere.

3.1 Selecting influential variables

To reduce the number of reaction rates, we pre-screen reactions for potential to change the rate of NO_x conversion to HNO_3. The aging rate (ΔA) is defined here as the slope of XNO_2:HNO_3 from parcel initiation (t_0) until the XNO_2:HNO_3 ratio is in the below the observed 75th quartile XNO_2:HNO_3 value ($t_{(75\,\%)}$). Figure 3 shows the transition point into the second quartile is defined as the first model output (at 30 min intervals) where the predicted XNO_2:HNO_3 is below the observed 75th percentile XNO_2:HNO_3. For the

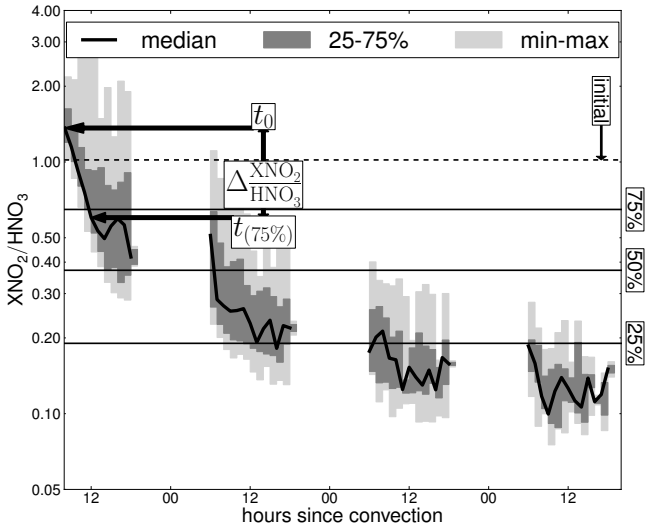

Fig. 3. XNO_2:HNO_3 (median: line; full range: light gray box; interquartile: dark gray box) plotted as a function of hours from simulation start. The observed XNO_2:HNO_3 quartiles are delineated by horizontal lines. Components of Eq. (1) are indicated with arrows.

pre-screening process, it is not practical to simulate the entire ensemble of air parcels. Instead, pre-screening uses a single air parcel with the initial conditions set to the median values from all initial air parcels. The median aging rate, from all air parcels, is approximately the same as the aging rate from one air parcel with median initial conditions. For each reaction, the median air parcel is simulated with the reaction rate set to $\pm 1\sigma$ uncertainty of the base rate. The base rates come from GEOS-Chem (v09-01-01) and uncertainty ranges are taken from IUPAC04, IUPAC06, and JPL06 (JPL11 became available after this work was completed). The uncertainty range used is the maximum when evaluated at 234 K, a typical temperature in the upper troposphere. For subsequent analysis using all initial conditions ($n = 65$), the 10 reaction rates that maximize the value of the negative aging slope (Eq. 1) are selected.

$$\Delta A = \frac{\left(\frac{XNO_2}{HNO_3}\right)_{t_{(75\,\%)}} - \left(\frac{XNO_2}{HNO_3}\right)_{t_0}}{t_{(75\,\%)} - t_0} \quad (1)$$

3.2 Bayesian updating

Each of the pre-screened reaction rates is influential and has a range of possible values that need to be evaluated. Each possible value can be evaluated in the upper troposphere to provide evidence that supports or refutes its use in upper tropospheric conditions. The evidence from model evaluation is incorporated using Bayesian inference, which is a quantitative method to refine uncertainty in model parameters. Bayesian inference, described in Eq. (2), can be summarized as updating the prior uncertainty distribution (hereafter "prior", $P(H)$) of model parameters by using the probability distribution (P) of evidence (E) given a hypothesis (H), hereafter "likelihood" (as in Dilks et al., 1992). In this case, we are updating prior uncertainty in kinetic rate coefficients based on the ability of the model to predict observations. The prior uncertainty for rate constants comes from literature (IUPAC04; IUPAC06; JPL06). The likelihood is a conditional probability that describes the probability of the observations given the model's predictive ability. The model's predictive ability is a function of its input parameters, including reaction rates. The likelihood, in this case, must be developed from populations of predictions and observations.

$$P(H|E) = \frac{P(E|H)P(H)}{P(E)} \quad (2)$$

Bayesian updating has previously been used for air quality model uncertainty analysis (Bergin and Milford, 2000), but the likelihood estimation must be updated for this study. Bergin and Milford (2000) evaluated uncertainty of a Lagrangian air quality model by adjusting model inputs within their uncertainty. Each adjusted model input creates a new model instance. The likelihood of a model instance ($L(o|y_k)$) characterizes the likelihood of that instance's input parameters. The likelihood of each instance is calculated based probability of observed (o) ozone mixing ratios given predicted ozone (y) paired in time and space. The likelihood (L) is then calculated, following Dilks et al. (1992), by assuming a normally distributed error in the prediction. Using this approach, the standard deviation used in the likelihood is the observational standard deviation. This assumption allows the likelihood to be calculated using a typical normal probability function. The likelihood formulation described above is unsuitable for this study because the observations are not paired in space and time to predictions, and the likelihood calculation should use the standard deviation of the predictions which are known in this study.

Instead of space/time-paired results, the observation set ($O = \{o_1, \ldots o_n\}$) and prediction ensembles ($Y = \{y_1, \ldots y_m\}$) are unpaired distributions that characterize the upper troposphere. Observations come from the INTEX-A DC-8 aircraft samples that have been merged into a 10-s merged dataset. In 10 s, the aircraft travels 1.5 to 3 km, which makes the observations effectively independent. The model framework (described in Sect. 2) is then used to generate simulated air parcels. For each reaction, 21 model instances are created by adjusting the rate coefficient (θ). Each model instances scales the rate coefficient to one of 21 values evenly spaced within the reported $\pm 3\sigma$ log-normally distributed uncertainty. The prediction ensemble from each model instance ($\{Y_1, \ldots, Y_{21}\}$) is then used to calculate the rate coefficient's likelihood ($L(O|\theta_k)$).

The likelihood can be calculated from the observed and simulated distributions of a species using the Dirichlet function. The Dirichlet function calculates a likelihood from a single probability mass function (PMF) (Frigyik et al., 2010). For use with the Dirichlet function, a single PMF is generated

by integrating the simulated distribution between observational quantiles (see Appendix A4). When the observed and simulated distributions are most similar, the PMF will be most uniform. When the PMF is most uniform, the Dirichlet likelihood is maximized.

Maximizing the likelihood of a single species could degrade the model performance for other species. For instance, adjusting a reaction rate (e.g., $NO_2 + HO^\bullet$) may decrease bias in one species (e.g., NO_2) while creating bias in another (e.g., O_3). To ensure that model improvements for one species do not come at the expense of another, likelihoods from multiple species (s) are combined. By combining multiple predicted species, the overall evaluation will be improved. For this study, the likelihood of reaction rates are calculated from five species or species ratios. First, XNO_2 and HNO_3 are selected because the model must produce the distributions coincidently to correctly simulate the upper troposphere. Second, the ratio of $HO_2^\bullet$:$HO^\bullet$ is chosen because it has been identified as an indicator of chemical uncertainty in the upper troposphere (Ren et al., 2008). Third, the $HO^\bullet$ is selected to constrain the absolute values of $HO_2^\bullet$ and $HO^\bullet$. Finally, O_3 is selected because of its importance in radiative forcing and air quality. For species with log-distributed observations (XNO_2, HNO_3, $HO_2^\bullet$:$HO^\bullet$), the observed and simulated values are log-transformed for the likelihood calculations.

The likelihood of any simulated species requires the specification of the average time-since-convection (τ) used by the model framework. For instance, as the value of τ increases, simulated nitric acid and ozone increase, thus improving or degrading the likelihood value. The likelihood of each model instance is calculated with each τ in the range of estimates (36–58). Equation (3) combines likelihoods from each τ and each selected species ($S = \{XNO_2, HNO_3, O_3, HO_2^\bullet : HO^\bullet, HO^\bullet\}$) to provide an overall likelihood for each model instance. The influence of τ is not considered to be refining, so the likelihood distribution is calculated as a function of uncertainty in each reaction by evaluating Eq. (3) for each of the 21 model instances (k) for that reaction (θ) scaled by uncertainty.

$$L(O|\theta_k) = L(O|Y_k) = \sum_{\tau=36}^{58} \prod_{s \in S} L(O_s|Y_s(\theta_k, \tau)) \quad (3)$$

The likelihood distribution of each reaction can then be combined with the prior (π) to produce the posterior uncertainty distribution. The posterior is the product of the likelihood and prior that has been normalized by the sum-product of the likelihood and prior (see Eq. 4). Once normalized, the posterior provides a revised estimate of the reaction's rate coefficient and its uncertainty.

$$P(\theta_k|O) = \frac{L(O|\theta_k)\pi(\theta_k)}{\sum_k L(O|\theta_k)\pi(\theta_k)} \quad (4)$$

Each reaction's estimate and uncertainty is further analyzed to identify spurious results. Spurious results occur when the likelihood of a reaction increases (or decreases) throughout the entire tested range. A monotonically increasing (or decreasing) likelihood can indicate one of two issues. First, the tested range may not include the true value for the rate coefficient. Second, the variable could have an effect that does not *meaningfully* improve model performance. In either case, the peak likelihood has not been identified and the posterior cannot be normalized for use in Bayesian estimation. To consider a peak bounded by the test, two decreasing values are required on either side of the peak likelihood.

The inferred rate from Bayesian inference will only be accepted when the original rate is unlikely given the inferred uncertainty distribution. For each reaction, the likelihood values will be used to estimate the Bayesian confidence interval or credible interval. When the 95 % credible interval does not include the original rate, the original rate is rejected and the revised estimate is recommended.

4 Results

4.1 Reaction pre-screening

The pre-screening selected 10 reactions that most influence the ratio of XNO_2 to HNO_3. Table 1 shows that the most influential reactions are a combination of inorganic, methane, and formaldehyde reactions that either directly oxidize or reduce NO_x or influence radical cycling. In addition to the ten reactions identified, $HO_2^\bullet + NO$ was also evaluated because it has been identified in several recent uncertainty analyses as a candidate for future research (e.g., Chen and Brune, 2010). The most influential reaction was the forward rate of $CH_3O_2^\bullet + NO_2 \xrightarrow{k_f} CH_3O_2NO_2$ (R10) with a ΔA of -0.342. The production of $CH_3O_2NO_2$ only temporarily removes a radical and a nitrogen dioxide. As the air parcel subsides and temperature increases, the methyl peroxy radical and nitrogen dioxide reenter the NO_x cycle. Given the inter-twined relationship between methyl peroxy nitrate's forward rate and equilibrium rate, the equilibrium rate was added to the list. The production of nitric acid (R12), though less influential with respect to ΔA, effectively removes a radical and a nitrogen dioxide from the cycles because nitric acid is chemically stable in the upper troposphere.

4.2 Bayesian estimation

Of the twelve tested reactions, this study was able to constrain uncertainty for four rate coefficients. For each of the four rate coefficients, the posterior uncertainty distributions are shown in a panel of Fig. 4. Each panel shows the probability of the reaction rate as a function of the uncertainty scaling factors tested. The scaling factors cover $\pm 3\sigma$ uncertainty with the base rate shown with a scaling factor of unity. Each panel also shows a log-normal parameterization ($\log\mathcal{N}(\mu, \sigma)$) where the mean ($\mu$) is the inferred scaling

Table 1. Maximum sensitivity of nitrogen aging (ΔA s^{-1}) to uncertainty in reaction rates.

Reaction	Uncertainty Factor @ 234 K IUPAC	JPL	ΔA
(R10) $CH_3OO^\bullet + NO_2 \xrightarrow{k_f} CH_3O_2NO_2$	N/A	1.282	−0.342
(R3) $NO + O_3 \rightarrow NO_2$	1.207	1.322	−0.358
(R1) $NO_2 \xrightarrow{h\nu} O_3 + NO$	N/A	1.200	−0.441
(R12) $NO_2 + OH \rightarrow HNO_3$	N/A	1.194	−0.444
(R13) $HNO_4 + OH \rightarrow NO_2$	1.373	2.059	−0.460
(R5) $CH_3OO^\bullet + NO \rightarrow NO_2 + HO_2 + CH_2O$	1.111	1.261	−0.463
(R10) $CH_3O_2NO_2 \xrightarrow{k_e^{-1}} NO_2 + CH_3OO^\bullet$	N/A	1.435	−0.466
(R6) $CH_2O \xrightarrow{h\nu} 2\,HO_2 + CO$	N/A	1.400	−0.466
(R14) $HO_2 + OH \rightarrow H_2O + O_2$	1.235	1.345	−0.471
(R7) $CH_4 + OH \rightarrow CH_3OO^\bullet + H_2O$	1.151	1.206	−0.472
(R8) $CH_3OOH + OH \rightarrow 70\,\% \; CH_3OO^\bullet + 30\,\% \; (CH_2O + OH)$	1.179	1.607	−0.474
(R4) $HO_2 + NO \rightarrow OH + NO_2$	1.179	1.204	−0.476

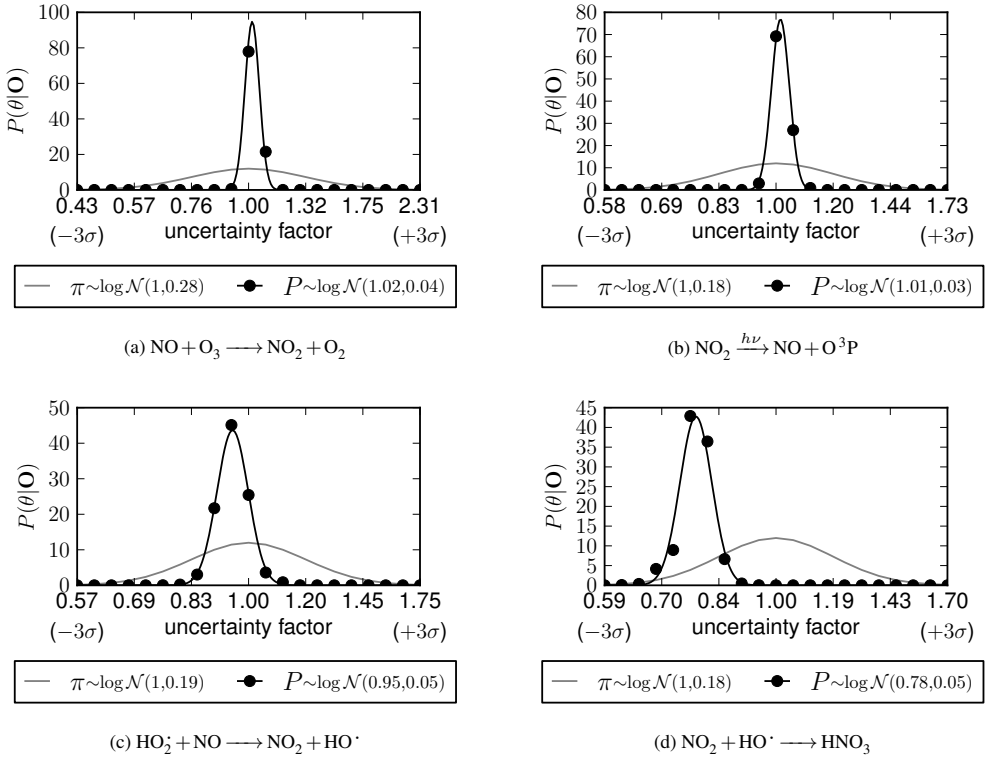

(a) $NO + O_3 \longrightarrow NO_2 + O_2$ (b) $NO_2 \xrightarrow{h\nu} NO + O\,^3P$

(c) $HO_2^\bullet + NO \longrightarrow NO_2 + HO^\bullet$ (d) $NO_2 + HO^\bullet \longrightarrow HNO_3$

Fig. 4. Posterior (black) and prior (gray) uncertainty distributions of selected reactions. Posterior distributions are explicitly calculated at 21 points shown by black squares, and the smoothed line is fit from the mean and standard deviation.

factor, and standard deviation (σ) is calculated from the posterior. For three reactions, the credible interval includes the base rate, but the uncertainty range has been reduced. The base rate coefficients for photolysis of NO_2 (R1) and oxidation of NO by O_3 (R3) were confirmed with inferred scaling factors within 2 % of unity. For the oxidation of NO by $HO_2^\bullet$ (R4), Fig. 4c shows that the posterior estimate of the scaling factor (0.95) falls within 5 % of unity. For these reactions, however, Fig. 4b–c show that the prior standard deviation has been reduced by 72 to 91 %.

The estimate and standard deviation have both been substantially revised for the production of HNO_3. For HNO_3 production, Fig. 4d shows that the revised rate coefficient is 22 % lower (within 1σ) than the base rate from JPL06 and

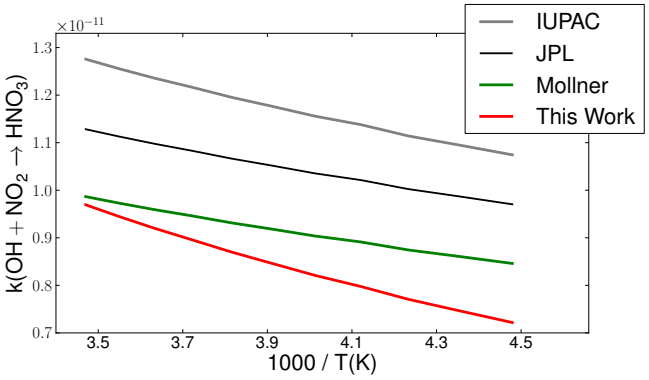

Fig. 5. Evaluated NO_2 + $HO^\bullet$ rate coefficients from IUPAC04 (IUPAC), JPL11 (JPL), Mollner et al. (2010) (Mollner), and this work for temperatures and pressures from the US standard atmosphere 1976.

the standard deviation has been reduced by 62 %. Based on the log-normal uncertainty, the 95 % credible interval for the revised rate is 66–85 % of the base rate.

5 Discussion

This study has constrained the uncertainty of reaction rates using observational data from the INTEX-A campaign. The reaction rates are constrained using Bayesian inference and an observational modeling system that calculates likelihoods from multiple endpoints, and are combined to constrain reactions that affect multiple species. The results indicate the need for a substantial revision of the rate of nitric acid production.

The inference results for nitric acid production (R12) show that current rate (JPL11; IUPAC04) is overestimated by 22–30 % in the upper troposphere. This finding agrees well with emerging laboratory studies by Mollner et al. (2010), who found that experimental artifacts have led to overestimation of the reaction rate. In their supplementary material, Mollner et al. (2010) fit their latest data to the existing (JPL06) temperature dependencies because their experiments were all performed at 298 K. Figure 5 shows that for all altitudes and temperatures in this study (227–251 K), their recommendation evaluates lower than the current best estimate by 13–21 % (JPL11-IUPAC04). Our findings in the upper troposphere suggest a further 12 % reduction compared to Mollner et al. (2010), which was only evaluated at 298 K.

The 12 % discrepancy is interpreted as a revision to the temperature sensitivity of the rate coefficient. The rate coefficient for HNO_3 production is pressure dependent with high-pressure and a low-pressure limit rate, but only the low-pressure limit ($k_{R12,low}$) has a temperature dependency. The temperature dependency of the low-pressure limit has been adjusted to fit the 298 K rate from Mollner et al. (2010) and the inferred rate from this study (Eq. 5).

$$k_{R12,low} = 1.49 \times 10^{-30} \times \left(\frac{T}{300}\right)^{-1.8} \quad (5)$$

The update to the temperature dependency may relate to emerging literature on HO_x/NO_x reactions. For instance, a second channel for the $HO^\bullet$ + NO_2 reaction forms isomers of HOONO (Nizkorodov and Wennberg, 2002). These isomers can photolyze or dissociate to reform $HO^\bullet$ and NO_2 thereby reducing the net forward reaction rate. The formation rate is temperature dependent (Bean et al., 2003), as is the fate. Given the uncertainty in fate, HOONO is not explicitly simulated in this study although HOONO may contribute to the findings here. Also the formation of HNO_3 from $HO_2^\bullet$ + NO (e.g., Butkovskaya et al., 2005), has the potential to further reduce the inferred (R12) value. The inference framework in this study uses a univariate approach that will not account for updates to multiple uncertain rates. Updates to recommended rates, which are used as the base mechanism for this paper, could alter the inference values reported here.

The decreased nitric acid formation rate has important implications for the nitrogen oxides (NO_x) and hydrogen radical (HO_x) budgets. For NO_x, slowing the formation of HNO_3 will increase the atmospheric lifetime and NO_x concentrations. Increasing NO_2 concentrations will help to remove previous model bias in comparison with aircraft and satellite observations. Revising this reaction, however, may also affect the $HO_2^\bullet$:$HO^\bullet$ ratio that Ren et al. (2008) identified as problematic above 8 km.

This study recommends updating the nitric acid formation reaction rate. Updating the NO_2 + $HO^\bullet$ reaction will lengthen NO_x lifetimes and increase ozone production (based on preliminary results). The full implications of this revision, however, cannot be evaluated in the model framework used here. In this model framework, unlike a chemical transport model, the air parcels are initiated by observations. In a chemical transport model, air parcels lofted to the upper troposphere entrain air from previously simulated upper troposphere. Any bias, therefore, has the potential to be cumulative and must be tested in a full chemical transport model to understand the implications. Previous laboratory and master equation estimates of the temperature sensitivity are in relatively good agreement (Sander et al., 2011). Given the improved measurement capabilities (Mollner et al., 2010) and remaining uncertainty (Donahue, 2011), the temperature sensitivity of the rate coefficient should be revisited in laboratory experiments.

Appendix A

A1 Observation summary

Table A1 gives descriptive statistics for environmental conditions and inorganic concentrations for all observations in the

Table A1. Summary of inorganic observations and environmental conditions, from 8 to 10 km, used for evaluation (all) and for initialization (initial, i.e., samples with the highest 12.5 % XNO_2 to HNO_3 ratios) from the INTEX-A observational campaign. Unless otherwise noted, values are in parts per trillion (ppt).

	all				initial			
Species	Median	Mean	Std	N	Median	Mean	Std	N
RH (%)	39.9	46.2	22.1	506	65.3	57.4	24.6	64
TEMP (K)	241.0	240.1	5.0	506	235.3	236.4	5.2	64
PRESS (hPa)	314.7	314.1	22.2	506	300.7	303.3	22.1	64
SO_2	19.9	32.7	60.3	493	20.4	57.2	125.8	64
$HO^{\bullet}$	0.6	0.6	0.2	481	0.6	0.7	0.3	62
$HO_2^{\bullet}$	13.6	13.7	3.7	506	13.0	12.8	3.8	64
H_2O_2	253.6	281.3	156.1	506	194.3	265.4	162.4	64
NO_2	83.9	102.2	75.4	506	137.3	153.7	101.3	64
HNO_3 (CalTech)	303.8	457.0	464.1	506	156.0	155.8	105.7	64
HNO_4	97.6	97.1	37.9	442	79.0	87.6	30.8	56
O_3 (ppb)	78.7	80.9	16.8	506	70.2	68.8	9.4	64
CO (ppb)	100.2	104.2	16.0	506	107.6	108.4	10.6	64

Table A2. Summary of organic observations, from 8 to 10 km, used for evaluation (all) and for initialization (initial) from the INTEX-A observational campaign. Unless otherwise noted values, are in parts per trillion (ppt).

	all				initial			
Species	Median	Mean	Std	N	Median	Mean	Std	N
CH_4 (ppb)	1793.0	1794.8	16.6	157	1784.0	1786.2	10.3	16
CH_3OH	1913.3	2008.2	871.3	236	3248.8	3370.4	645.1	24
CH_3OOH	133.0	139.0	98.4	169	233.0	205.8	94.4	31
CH_2O	193.0	233.9	186.6	332	437.0	422.1	158.6	29
C_2H_6	839.0	940.9	393.1	251	830.0	809.1	265.1	29
C_2H_4	1.5	3.5	7.7	252	1.5	6.5	8.2	29
C_2H_2	82.0	91.9	32.0	251	97.0	99.5	22.9	29
$CH_3C(O)H$	111.4	127.4	113.2	228	87.8	95.4	40.1	24
CH_3CH_2OH	35.7	81.9	93.2	219	260.6	251.4	73.7	24
$CH_3C(O)OOH$	212.8	211.5	77.7	492	230.1	207.9	74.0	62
C_3H_8	185.0	244.9	215.7	251	171.0	180.2	93.7	29
C_4H_{10}	46.0	70.6	77.1	251	53.0	66.0	33.8	29
C_5H_{12}	11.0	17.0	18.8	252	15.0	23.8	20.0	29
n-Hexane	1.5	2.0	1.7	252	1.5	2.3	2.3	29
$CH_3C(O)CH_3$	1600.4	1767.7	661.8	236	1374.7	1485.6	296.1	24
$CH_3C(O)CH_2CH_3$	78.8	84.6	38.2	236	94.0	89.2	16.4	24
PAN	397.1	441.7	172.2	506	369.8	385.1	144.8	64
CH_3ONO_2	2.2	2.2	0.3	251	2.4	2.3	0.3	29
$RONO_2^*$	8.4	10.6	7.6	251	6.5	7.9	3.2	29

* Sum of nitrates is unavaible; $RONO_2$ is the sum of speciated nitrates.

upper troposphere (all) and also for just those used for initial conditions. Observations (all and initial) have been filtered to exclude biomass burning, stratospheric influence, and extreme pollution (as in Hudman et al., 2007; Henderson et al., 2011). Table A2 gives descriptive statistics for organic concentrations for all observations in the upper troposphere (all) and also for just those used for initial conditions. Table A3 gives descriptive statistics for aerosol composition measurements for all observations in the upper troposphere (all) and also for just those used for initial conditions.

A2 Dynamic environmental conditions

Gas phase concentrations evolve as a function of their environmental conditions. Temperature, pressure, and relative

Table A3. Summary of aerosol observations, from 8 to 10 km, used for evaluation (all) and for initialization (initial) from the INTEX-A observational campaign. Unless otherwise noted values, are in parts per trillion (ppt).

	all				initial			
Species	Median	Mean	Std	N	Median	Mean	Std	N
NO_3^-	11.0	14.6	16.3	116	18.0	19.3	15.9	33
$SO_4^=$	44.0	56.3	28.4	116	66.0	69.6	27.6	33
Na^+	43.5	77.2	76.5	116	43.5	119.9	108.8	33
NH_4^+	59.0	66.3	46.4	116	71.0	84.1	26.7	33
Mg^{2+}	3.5	3.8	3.7	116	3.5	3.5	0.0	33
K^+	14.0	26.3	27.4	116	14.0	41.2	38.2	33
Ca^{2+}	4.0	9.9	19.5	116	4.0	10.8	12.6	33
Cl^-	30.0	80.3	89.0	116	30.0	80.5	74.2	33

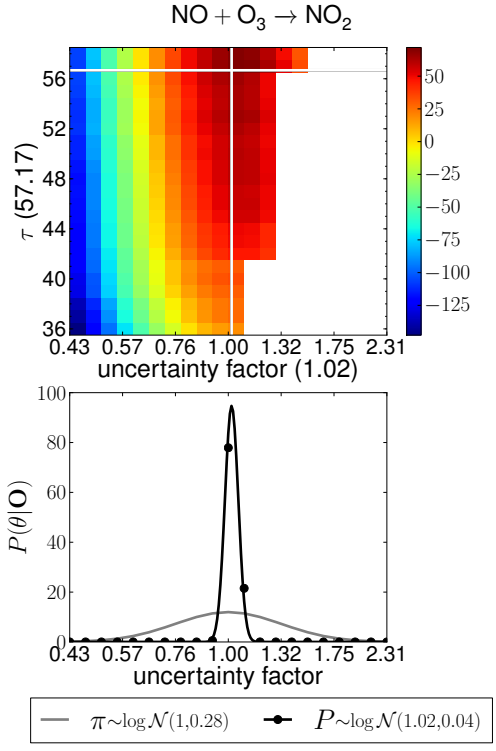

Fig. A1. Posterior distribution in two dimensions (color plot) and integrated for all tested τ valus (line plot) for the $NO + O_3 \rightarrow NO_2 + O_2$ reaction. The two dimensional posterior distribution as a function of uncertainty in the rate and time-since-convection (τ). On the two-dimensional posterior plots, the inferred values of τ and the reaction rate scaling factor are in parentheses. The one dimensional posterior distribution is as a function of the reaction rate uncertainty. On the one-dimensional posterior plot, the line is a smoothed uncertainty using the inferred estimate and standard deviation to construct a log-normal uncertainty. When the log-posterior is white, it was incalculably small ($-\infty$).

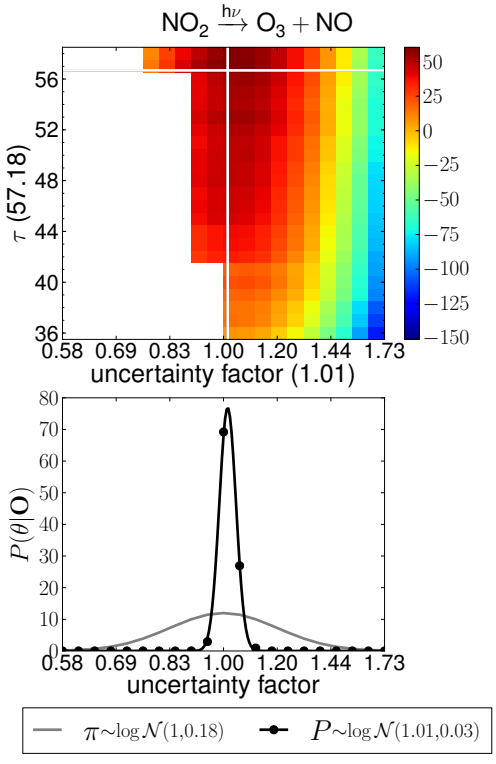

Fig. A2. Same as Fig. A1 for the $NO_2 \xrightarrow{h\nu} NO + O^3P$ reaction.

humidity drive reaction rates (gas-phase and heterogeneous) and thermal partitioning of to aerosols. The difference is driven by adiabatic cooling or warming and mixing with background air. The rates of adiabatic processes are not well understood, but are thought to occur within an hour.

In this study, we see that environmental conditions in initial air parcels are distinct from the base conditions. The initial conditions are taken from samples with the highest XNO_2:HNO_3 ratios (top 12.5 %). The initial conditions are

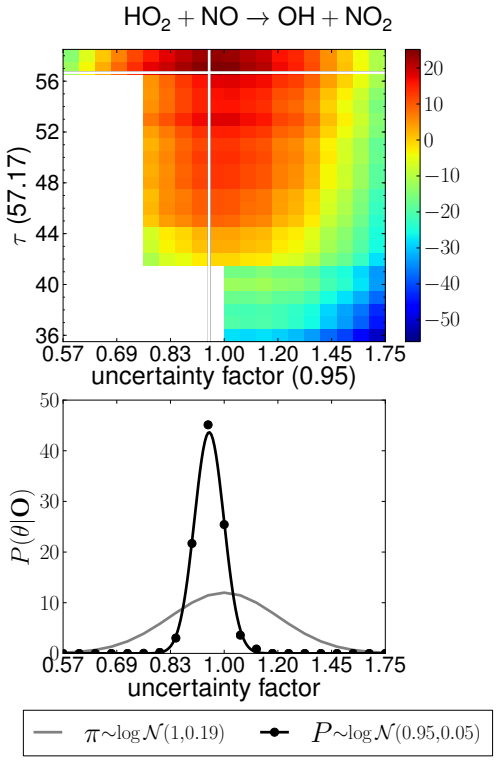

Fig. A3. Same as Fig. A1 for the $HO_2^{\bullet} + NO \rightarrow NO_2 + HO^{\bullet}$ reaction.

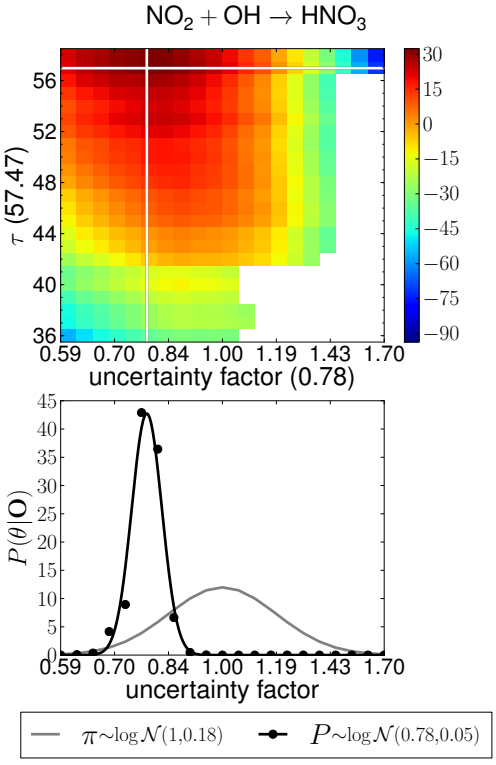

Fig. A4. Same as Fig. A1 for the $NO_2 + HO^{\bullet} \rightarrow HNO_3$ reaction.

not statistically different from the first quartile (top 25 %) of samples, but are different from the second quartile. The second quartile is not statistically different from the base conditions. Based on this observation, temperature, pressure, and relative humidity are parameterized to adjust from their initial to their "bulk" condition after the predicted XNO_2:HNO_3 ratio drops below the average second quartile value. The air parcels adjusted property (temperature, pressure, humidity) reduced or increased by the difference between median initial and median base conditions. The new property is not allowed to exceed the maximum or drop below the minimum value of the base property.

A3 Nitrogen dioxide and interference

Incorporating the findings from Browne et al. (2011) requires adjusting the NO_2 measurement as well as adding reactions to the chemical mechanism. Browne et al. (2011) found that the NO_2 measurement has interferences from HNO_4 and methyl peroxy nitrate (MPN). The GEOS-Chem chemical mechanism already includes HNO_4, but it does not include MPN. The MPN chemistry from JPL06 is incorporated with the assumption that the photolysis rate are similiar to HNO_4 (as in Browne et al., 2011). The impact of the adding MPN chemistry was then confirmed to be small by itself.

To adjust the NO_2 the measurement, the interference from MPN and HNO_4 must be removed. The INTEX-A campaign included measurements of HNO_4, but MPN will have to be estimated. The estimate of MPN is not straight forward because the concentrations may not be at steady-state results for air parcels immediately following convection. To estimate MPN, the model is run for all air parcels for 1 h using the original initial conditions. The output MPN results are used for least squares regression to estimate the fraction of the NO_2 measurement that MPN is as a function of NO_2:HNO_3. Using that relationship, a new set of initial conditions are created with MPN and with "corrected" NO_2. Those initial conditions are used to repeat the above process. Based on the second least squares regression, the MPN concentrations are estimated in the initial conditions using Eq. (A2). To avoid relying on derived observations, all subsequent analysis uses the TD-LIF measurement (XNO_2) and compares to the simulated value ($XNO_2 = NO_2 + 62.5\,\%\ MPN + 4.5\,\%\ HNO_4$).

$$\mathrm{MPN} = \left(2.05832508 \times 10^{-01} + 6.41325760 \times 10^{-06} \cdot \mathrm{XNO_2}/\mathrm{HNO_3}\right) \cdot \mathrm{XNO_2} \quad \text{(A1)}$$

$$\mathrm{NO_2} = \mathrm{XNO_2} - 62.5\,\%\ \mathrm{MPN} - 4.5\,\%\ \mathrm{HNO_4} \quad \text{(A2)}$$

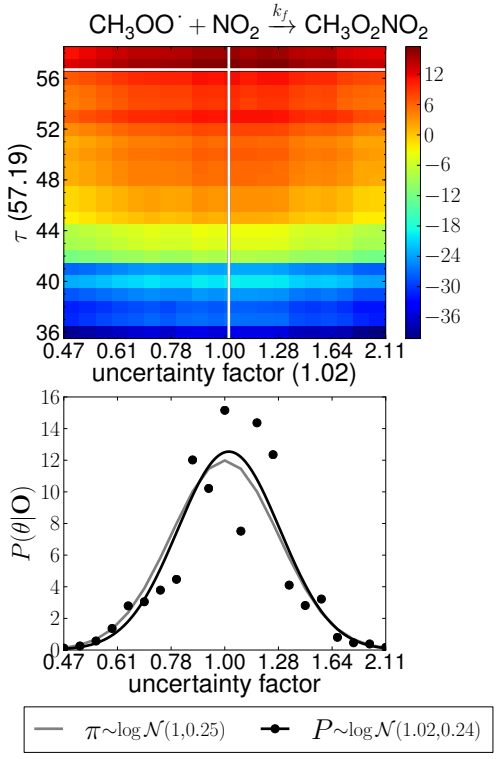

Fig. A5. Same as Fig. A1 for the $CH_3O_2^{\bullet} + NO_2 \rightarrow CH_3O_2NO_2$ reaction.

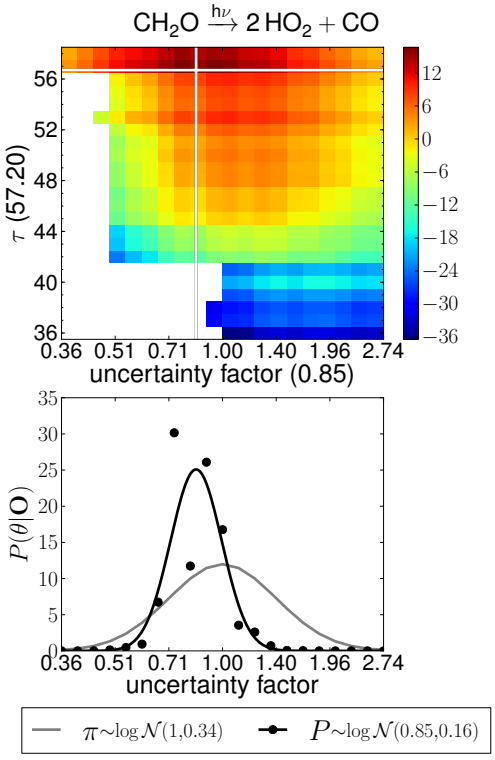

Fig. A6. Same as Fig. A1 for the $CH_2O + h\nu$ reaction.

A4 Dirichlet likelihood

The likelihood of a model instance is calculated from the observed and simulated distributions using the Dirichlet probability density function. The Dirichlet probability density function (PDF) calculates the likelihood based on discrete probabilities (Frigyik et al., 2010). A single discrete probability (PDF) is constructed by integrating between from the quantiles (i.e., ordered samples $O = \{o_{(1)}, ..., o_{(n)}\}$) of observations and PDF of the simulation results from a model instance. For each model instance (k), the PDF of predictions ($Y = \{y_1, ..., y_m\}$) can be estimated using a Gaussian Kernel Density Estimation. Equation (A3) describes the PDF where k is the model instance, m is the number of observations, h is the bandwidth is calculated following. The bandwidth is calculated following Scott (1992, $h = m^{-\frac{1}{5}}\sigma$). The PDF can then be calculated as the integral of the PDF between two observations $(o_i, o_{i+1}]$, as described in Eq. (A4).

$$\hat{f}(x|Y_k) = \frac{1}{mh}\sum_{i=1}^{m}\frac{1}{\sqrt{2\pi}}\exp\left(-\frac{1}{2}\left(\frac{x-y_{k,i}}{h}\right)^2\right) \quad \text{(A3)}$$

$$\text{PDF} = \left(\int_{y=-\infty}^{o_{(1)}} \hat{f}(o)do, \ldots \int_{o_{(i)}}^{o_{(i+1)}} \hat{f}(o)do, \ldots \int_{o_{(n)}}^{\infty} \hat{f}(o)do\right) \quad \text{(A4)}$$

For each model instance (k), the likelihood of the actual PDF is described by Eq. (A5) where $\boldsymbol{\alpha}$ is the set of alpha values ($\{\alpha_1, ..., \alpha_{n+1}\}$). The alpha values determine shape of the Dirichlet distribution. When the alpha values are greater than 1, the distribution is convex and the mean coincides with the PDF being uniform and so the likelihood maximizes when PDF values are uniform between all quantiles. Given that quantiles are asymptotically distributed (Mosteller, 2006), the PDF values are expected to be uniform (i.e., $\approx 1/(n_{\text{obs}}+1)$) from the "true" model. Based on this, therefore, likelihood calculation uses alpha values greater than one to maximize the likelihood of model instances with uniform PDF between all observed quantiles.

$$L(O|Y) = \text{Dir}(\text{PDF};\boldsymbol{\alpha}) = \frac{\Gamma\left(\sum_{i=1}^{n+1}\alpha_i\right)}{\prod_{i=1}^{n+1}\Gamma(\alpha_i)} \cdot \prod_{i=1}^{n+1}\text{PDF}_i^{\alpha_i - 1} \quad \text{(A5)}$$

If the location of all quantiles were equally certain, the alpha values would be uniform. The exact location of quantiles in the tails of the observed distribution are more subject to random chance or measurement uncertainty (i.e., near lower limit of detection). The alpha values can be interpreted as one plus the number of observations of each quantile. To account for decreasing certainty in the location of quantiles near the distribution tails, the quantile (Q) is used to calculate weighted alpha values (α) as shown in Eq. (A6).

$$\alpha = 1 + Q\cdot(1-Q)\cdot 4\cdot Q = \frac{(1,2,\ldots n,n+1)}{(n+2)} \quad \text{(A6)}$$

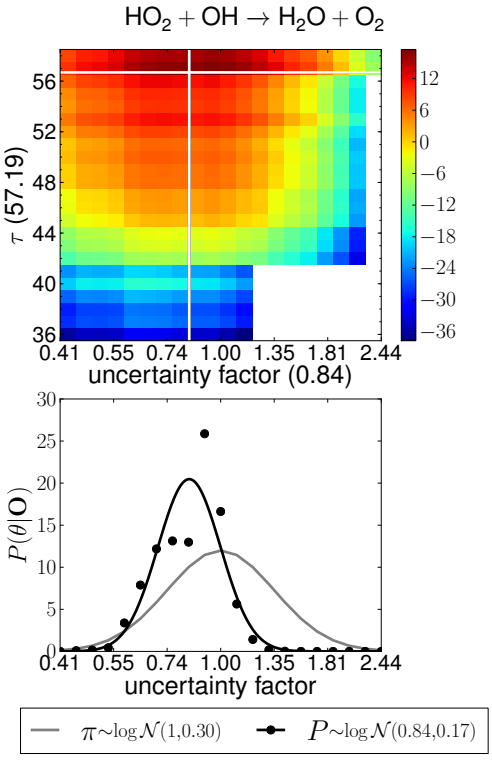

Fig. A7. Same as Fig. A1 for the $HO_2^{\bullet} + HO^{\bullet} \rightarrow H_2O + O_2$ reaction.

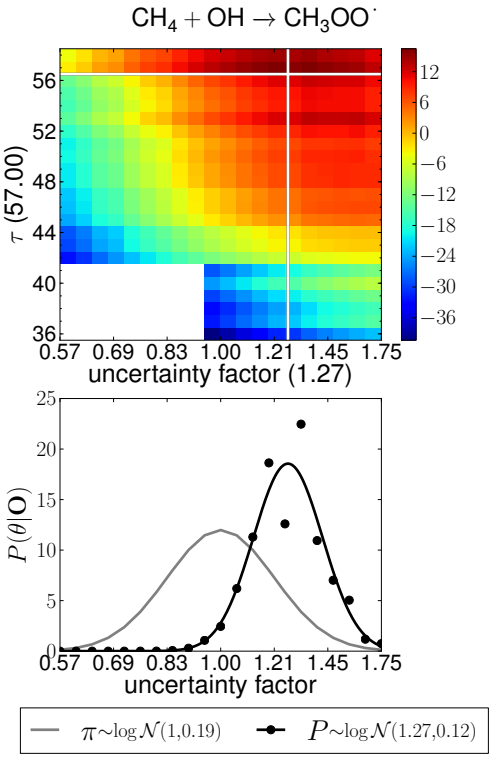

Fig. A8. Same as Fig. A1 for the $CH_4 + OH$ reaction.

A5 Likelihoods

The likelihood distribution of each reaction in the results was calculated as the joint likelihood from each species and as a function of average time-since-convection (τ). Figures A1–A8 show the joint likelihoods as a function of τ and reaction uncertainty. The results have been split into two categories: those that provided useful constraints and those that did not. Figures A1–A3 show three reactions whose the standard deviation has been substantially reduced. Figure A4 shows that the inferred rate and standard deviation have been substantially reduced for the production of nitric acid.

Figures A5–A8 shows the other reactions whose peak likelihood was bounded, but did not provide useful constraints. For these reactions, the 95 % confidence interval included the original rate and did not refine the uncertainty space. The probability distributions for these reactions have more than one mode.

Acknowledgements. Special thanks for DC8 observational data to Melody Avery, Donald Blake, William Brune, Alan Fried, Brian Heikes, Greg Huey, Glen Sachse, Hanwant Singh, and the INTEX team. Thank you to Ellie Browne for reviewing our methyl peroxy nitrate chemistry, to Paul Wennberg for helpful conversation about the upper troposphere, and to Golam Sarwar and William T. Hutzell for their input. Thank you to Gao Chen for helping identify and document the INTEX HO_x corrections, and to Mat Evans for help with the Dynamically Simple Model of Atmospheric Chemical Complexity.

This research was supported in part by an appointment to the Research Participation Program at the National Exposure Research Laboratory, US Environmental Protection Agency administered by the Oak Ridge Institute for Science and Education through an interagency agreement between the US Department of Energy and EPA.

Disclaimer. Although this paper has been reviewed by the EPA and approved for publication, it does not necessarily reflect EPAs policies or views.

Edited by: P. O. Wennberg

References

Allen, D. J., Pickering, K. E., Pinder, R. W., Henderson, B. H., Appel, K. W., and Prados, A.: Impact of lightning-NO on Eastern United States photochemistry during the summer of 2006 as determined using the CMAQ model, Atmos. Chem. Phys. Discuss., 11, 17699–17757, doi:10.5194/acpd-11-17699-2011, 2011.

Atkinson, R., Baulch, D. L., Cox, R. A., Crowley, J. N., Hampson, R. F., Hynes, R. G., Jenkin, M. E., Rossi, M. J., and Troe, J.: Evaluated kinetic and photochemical data for atmospheric chemistry: Volume I – gas phase reactions of O_x, HO_x, NO_x and SO_x species, Atmos. Chem. Phys., 4, 1461–1738, doi:10.5194/acp-4-1461-2004, 2004.

Atkinson, R., Baulch, D. L., Cox, R. A., Crowley, J. N., Hampson, R. F., Hynes, R. G., Jenkin, M. E., Rossi, M. J., Troe, J., and IUPAC Subcommittee: Evaluated kinetic and photochemical data for atmospheric chemistry: Volume II – gas phase reactions of organic species, Atmos. Chem. Phys., 6, 3625–4055, doi:10.5194/acp-6-3625-2006, 2006.

Bean, B. D., Mollner, A. K., Nizkorodov, S. A., Nair, G., Okumura, M., Sander, S. P., Peterson, K. A., and Francisco, J. S.: Cavity Ringdown Spectroscopy of cis-cis HOONO and the HOONO/$HONO_2$ Branching Ratio in the Reaction OH + NO_2 + M, J. Phys. Chem. A, 107, 6974–6985, doi:10.1021/jp034407c, 2003.

Bergin, M. and Milford, J.: Application of Bayesian Monte Carlo analysis to a Lagrangian photochemical air quality model, Atmos. Environ., 34, 781–792, 2000.

Bertram, T. H., Perring, A. E., Wooldridge, P. J., Crounse, J. D., Kwan, A. J., Wennberg, P. O., Scheuer, E., Dibb, J., Avery, M. A., Sachse, G. W., Vay, S. A., Crawford, J. H., McNaughton, C. S., Clarke, A., Pickering, K. E., Fuelberg, H., Huey, G., Blake, D. R., Singh, H. B., Hall, S. R., Shetter, R. E., Fried, A., Heikes, B. G., and Cohen, R. C.: Direct Measurements of the Convective Recycling of the Upper Troposphere, Science, 315, 816–820, doi:10.1126/science.1134548, 2007.

Browne, E. C., Perring, A. E., Wooldridge, P. J., Apel, E., Hall, S. R., Huey, L. G., Mao, J., Spencer, K. M., Clair, J. M. St., Weinheimer, A. J., Wisthaler, A., and Cohen, R. C.: Global and regional effects of the photochemistry of $CH_3O_2NO_2$: evidence from ARCTAS, Atmos. Chem. Phys., 11, 4209–4219, doi:10.5194/acp-11-4209-2011, 2011.

Butkovskaya, N. I., Kukui, A., Pouvesle, N., and Bras, G. L.: Formation of Nitric Acid in the Gas-Phase HO_2 + NO Reaction: Effects of Temperature and Water Vapor, J. Phys. Chem. A, 109, 6509–6520, doi:10.1021/jp051534v, 2005.

Chen, S. and Brune, W.: Sensitivity Analysis of the RACM Chemical Mechanism Based on TRAMP-2006 Field Data, UC Davis Atmospheric Chemical Mechanisms, 2010.

Davis, J. M., Bhave, P. V., and Foley, K. M.: Parameterization of N_2O_5 reaction probabilities on the surface of particles containing ammonium, sulfate, and nitrate, Atmos. Chem. Phys., 8, 5295–5311, doi:10.5194/acp-8-5295-2008, 2008.

Dilks, D., Canale, R., and Meier, P.: Development of Bayesian Monte Carlo techniques for water quality model uncertainty, Ecol. Modell., 62, 149–162, 1992.

Donahue, N.: Atmospheric chemistry: The reaction that wouldn't quit, Nat. Chem., 3, 98–99, 2011.

Evans, M. J. and Jacob, D. J.: Impact of new laboratory studies of N_2O_5 hydrolysis on global model budgets of tropospheric nitrogen oxides, ozone and OH, Geophys. Res. Lett., 32, L09813, doi:10.1029/2005GL022469, 2005.

Fountoukis, C. and Nenes, A.: ISORROPIA II: a computationally efficient thermodynamic equilibrium model for $K^+Ca^{2+}Mg^{2+}NH_4^+Na^+SO_4^{2-}$-$NO_3$-$Cl^-H_2O$ aerosols, Atmos. Chem. Phys., 7, 4639–4659, doi:10.5194/acp-7-4639-2007, 2007.

Frigyik, B. A., Kapila, A., and Gupta, M. R.: Introduction to the Dirichlet Distribution and Related Processes, Tech. Rep. UWEETR-2010-0006, Department of Electrical Engineering, University of Washington, 2010.

Fuelberg, H. E., Porter, M. J., Kiley, C. M., Halland, J. J., and Morse, D.: Meteorological conditions and anomalies during the Intercontinental Chemical Transport Experiment – North America, J. Geophys. Res., 112, 1–22, doi:10.1029/2006JD007734, 2007.

Gallager, R. G.: Discrete Stochastic Processes, Kluwer Academic Publishers, Boston/Dordrecht/London, 1996.

Henderson, B. H., Pinder, R. W., Crooks, J., Cohen, R. C., Hutzell, W. T., Sarwar, G., Goliff, W. S., Stockwell, W. R., Fahr, A., Mathur, R., Carlton, A. G., and Vizuete, W.: Evaluation of simulated photochemical partitioning of oxidized nitrogen in the upper troposphere, Atmos. Chem. Phys., 11, 275–291, doi:10.5194/acp-11-275-2011, 2011.

Hudman, R. C., Jacob, D. J., Turquety, S., Leibensperger, E. M., Murray, L. T., Wu, S., Gilliland, A. B., Avery, M., Bertram, T. H., Brune, W., Cohen, R. C., Dibb, J. E., Flocke, F. M., Fried, A., Holloway, J., Neuman, J. A., Orville, R., Perring, A., Ren, X., Sachse, G. W., Singh, H. B., Swanson, A., and Wooldridge, P. J.: Surface and lightning sources of nitrogen oxides over the United States: Magnitudes, chemical evolution, and outflow, J. Geophys. Res., 112, D12S05, doi:10.1029/2006JD007912, 2007.

Jacob, D.: Heterogeneous chemistry and tropospheric ozone, Atmos. Environ., 34, 2131–2159, 2000.

Jaeglé, L., Jacob, D., Wang, Y., and Weinheimer, A.: Sources and chemistry of NO_x in the upper troposphere over the United States, Geophys. Res. Lett., 25, 1705–1708, 1998.

Kley, D.: Tropospheric chemistry and transport, Science, 276, 1043–1045, doi:10.1126/science.276.5315.1043, 1997.

Madronich, S.: The Tropospheric Visible Ultra-violet (TUV) model web page, http://cprm.acd.ucar.edu/Models/TUV/, last access: 12 January 2012, 2002.

Mao, J., Carouge, C., Evans, M., Millet, D., and Palmer, P.: GEOS-Chem Chemical Mechanism Version 8-02-04, 2009.

Mollner, A. K., Valluvadasan, S., Feng, L., Sprague, M. K., Okumura, M., Milligan, D. B., Bloss, W. J., Sander, S. P., Martien, P. T., Harley, R. A., Mccoy, A. B., and Carter, W. P. L.: Rate of Gas Phase Association of Hydroxyl Radical and Nitrogen Dioxide, Science, 330, 646–649, doi:10.1126/science.1193030, 2010.

Mosteller, F.: On some useful "inefficient" statistics, Selected Papers of Frederick Mosteller, 69–100, 2006.

Napelenok, S. L., Pinder, R. W., Gilliland, A. B., and Martin, R. V.: A method for evaluating spatially-resolved NO_x emissions using Kalman filter inversion, direct sensitivities, and space-based NO_2 observations, Atmos. Chem. Phys., 8, 5603–5614, doi:10.5194/acp-8-5603-2008, 2008.

Nizkorodov, S. and Wennberg, P.: First spectroscopic observation of gas-phase HOONO, J. Phys. Chem. A, 106, 855–859, 2002.

Olson, J. R., Crawford, J., Chen, G., Brune, W. H., Faloona, I. C., Tan, D., Harder, H., and Martinez, M.: A reevaluation of airborne HO_x observations from NASA field campaigns, J. Geophys. Res.-Atmos., 111, D10301, doi:10.1029/2005JD006617, 2006.

Prather, M. and Jacob, D.: A persistent imbalance in HO_x and NO_x photochemistry of the upper troposphere driven by deep tropical convection, Geophys. Res. Lett., 24, 3189–3192, 1997.

Ren, X., Olson, J. R., Crawford, J. H., Brune, W. H., Mao, J., Long, R. B., Chen, Z., Chen, G., Avery, M. A., Sachse, G. W., BARRICK, J. D., Diskin, G. S., Huey, L. G., Fried, A., Cohen, R. C., Heikes, B. G., Wennberg, P. O., Singh, H. B., Blake, D. R., and Shetter, R. E.: HO_x chemistry during

INTEX-A 2004: Observation, model calculation, and comparison with previous studies, J. Geophys. Res., 113, 1–13, doi:10.1029/2007JD009166, 2008.

Sander, S., Friedl, R. R., Golden, D. M., Kurylo, M. J., Moortgat, G. K., Wine, P. H., Ravishankara, A. R., Kolb, C. E., Molina, M. J., Finlayson-Pitts, B. J., Huie, R. E., and Orkin, V.: Chemical Kinetics and Photochemical Data for Use in Atmospheric Studies Evaluation Number 15, JPL Publ., 2006.

Sander, S., Friedl, R., Abbatt, J., Barker, J., Golden, D., Kolb, C., Kurylo, M., Moortgat, G., Wine, P., and Huie, R.: Chemical Kinetics and Photochemical Data for Use in Atmospheric Studies Evaluation Number 17, JPL Publication 10-6, 2011.

Scott, D. W.: Multivariate Density Estimation: Theory, Practice, and Visualization, Wiley, 1992.

Solomon, S., Qin, D., Manning, M., Alley, R., Berntsen, T., Bindoff, N., Chen, Z., Chidthaisong, A., Gregory, J., Hegerl, G., Heimann, M., Hewitson, B., Hoskins, B., Joos, F., Jouzel, J., Kattsov, V., Lohmann, U., Matsuno, T., Molina, M., Nicholls, N., Overpeck, J., Raga, G., Ramaswamy, V., Ren, J., Rusticucci, M., Somerville, R., Stocker, T., Whetton, P., Wood, R., and Wratt, D.: Technical Summary, in: Climate Change 2007: The Physical Science Basis. Contribution of Working Group I to the Fourth Assessment Report of the Intergovernmental Panel on Climate Change, IPCC AR4, p. 74, 2007.

Wang, Y., Jacob, D. J., and Logan, J.: Global simulation of tropospheric O_3-NO_x-hydrocarbon chemistry 1. Model formulation, 1998.